# Micromechanical model for cohesive materials based upon pseudo-granular structure

Anil Misra, Yang Yang

## To cite this version:

Anil Misra, Yang Yang. Micromechanical model for cohesive materials based upon pseudo-granular structure. International Journal of Solids and Structures, 2010, 47 (21), pp.2970-2981. hal-00556078

## HAL Id: hal-00556078
## https://hal.science/hal-00556078

Submitted on 15 Jan 2011

# Micromechanical model for cohesive materials based upon pseudo-granular structure

Anil Misra [a,*], Yang Yang [a,b]

[a] Department of Civil, Environmental and Architectural Engineering, The University of Kansas, Learned Hall, 1530 W. 15th Street, Lawrence, KS 66045-7609, United States
[b] Faculty of Engineering, China University of Geosciences, Wuhan, Hubei, China

ARTICLE INFO

*Article history:*
Received 6 November 2009
Received in revised form 2 January 2010
Available online 11 July 2010

*Keywords:*
Micromechanics
Failure surface
Cohesive materials
Multi-scale modeling
Granular media

ABSTRACT

A micromechanical model for cohesive materials is derived by considering their underlying microstructure conceptualized as a collection of grains interacting through pseudo-bonds. The pseudo-bond or the inter-granular force–displacement relations are formulated taking inspiration from the atomistic-level particle interactions. These force–displacement relationships are then used to derive the incremental stiffnesses at the grain-scale, and consequently, obtain the sample-scale stress–strain relationship of a representative volume of the material. The derived relationship is utilized to study the stress–strain and failure behavior including the volume change and "brittle" to "ductile" transition behavior of cohesive materials under multi-axial loading condition. The model calculations are compared with available measured data for model validation. Model predictions exhibit both quantitative and qualitative consistency with the observed behavior of cohesive material.

## 1. Introduction

Cohesive materials, such as, ceramics, rocks and cementitious materials are important due to their wide applications in various fields of engineering. Accurate numerical models of the stress–strain behavior are necessary for correctly forecasting the damage and failure response of these materials. Stress–strain relations for cohesive materials have been traditionally established through direct phenomenological modeling based upon experimental observations, such as those done by van Mier and co-workers (1986, 1997), Ferretti (2004), Zhou et al. (2004) and many others. The stress–strain behavior of these materials is, generally, complex and critically depends upon the underlying mechanisms that occur at scales smaller than the material sample-scale. Therefore, modeling methodologies that account for the underlying mechanisms and explicitly model material microstructure are expected to provide better insight to the material stress–strain behavior. For instance, lattice models of concrete microstructure have been found useful for describing concrete fracture behavior by van Mier (1997). In the lattice models, the material microstructure is projected on a lattice network and the lattice elements are regarded as beams with appropriate properties. In addition to the lattice network models, there have been other numerous micromechanical models modeling cohesive material by considering mechanisms at different spatial scales. For instance, Chang and co-workers (Chang and Misra, 1990; Chang and Lun, 1992; Chang and Liao, 1994; Chang and Gao, 1996; Hicher and Chang, 2005) have derived constitutive relations based on the microstructure for elastic properties of the granular material. Jefferson et al. (2002) have presented a discrete particle model which provides an improved estimate for the effective elastic response of cohesive elastic aggregates undergoing homogeneous deformation. Furthermore, Bažant and co-workers have presented microplane model that has been successfully applied to model concrete fracture and anelasticity (Bažant and Caner, 2005). Granular or discrete microstructure models of cohesive material damage/failure have also been considered in the past, such as the virtual internal bond (VIB) model by Gao and Klein (1998), which, suffers from the limitation of fixed Poisson's ratio. To address this limitation, the VIB model has been further developed (cf. Lin and Shu, 2002; Zhang and Ge, 2005, 2006, 2008 among others. Microstructural models have also been developed to model elasto-plastic and damage behavior of granular materials with friction and adhesive grain interactions (Chang and Hicher, 2005; Hicher et al., 2008). Furthermore, Chang and co-workers (2002) have developed higher-order constitutive relationships which can successfully model softening behavior of granular media by relating higher-order stress terms to the higher-order strain terms.

In this paper we have utilized a microstructural mechanics approach used in granular mechanics to model the stress–strain and failure behavior of cohesive materials. We have considered monolithic materials with microstructure to be divided into grains whose centroids represent material points. In analogy with atomic-scale interactions, these grains are viewed as interacting with

---

* Corresponding author. Tel.: +1 785 864 1750; fax: +1 785 864 5631.
*E-mail address:* amisra@ku.edu (A. Misra).

each other through pseudo-bonds. In this sense, the model has similarity with the VIB model (Gao and Klein, 1998), which uses "cohesive bonds" to represent interactions between material points. However, since the pseudo-bonds describe the behavior of collection of atoms, therefore, the interactions represented by these bonds are quite complex. Consequently, the force-laws that describe the behavior of pseudo-bonds have to be crafted in a manner that captures the essential features of grain interactions as was conceptually discussed by Misra et al. (2003). In the present paper, we have formulated generalized pseudo-bond force-laws that can describe both the normal and tangential inter-granular behavior. The overall constitutive law of the material is then obtained by averaging over the random network formed by the pseudo-bonds. In general, the averaging process requires the relationships between local variables (such as inter-granular forces and displacements) and global variables (such as element stress and strains). For simplicity, the local variables are obtained in terms of the global variables by either kinematic assumption or the static assumption. These assumptions have been widely discussed in the microstructural granular mechanics literature. In the present paper, we have utilized the kinematic assumption. The model we have presented provides similar advantages that the models of this genre possess (Chang et al., 2002; Bažant and Caner, 2005). Using the derived micromechanical model, we can explain the macro-scale behavior of cohesive material under multi-axial tensile and compressive loads, even though we have employed relatively simple descriptions of inter-granular behavior.

In the subsequent discussion, we first describe the overall methodology including the projection of a physical continuum model to a discrete granular structure as well as the formulation of force–displacement relations inspired by the atomic-scale interactions. This is followed by brief description of the constitutive modeling and the derivation of closed form of constitutive relationships for the idealized granular system under initial infinitesimal load. The model applicability is then evaluated by comparison of the calculated stress–strain relations as well as the failure behavior to the available experimental data under uniaxial, biaxial and triaxial loading conditions.

## 2. Continuum idealized as granular system

We consider monolithic materials with microstructure to be divided into grains whose centroids represent material points as depicted in Fig. 1. Under an applied load on a sample of such a material, the conceptual grains may translate or rotate. Considering each grain to have six degrees of freedom, i.e., three translational and three rotational degrees of freedom, the relative displacement, $\delta_i$, between two nearest neighbor grains $n$ and $p$ (see Fig. 1) is given by Misra and Chang (1993).

$$\delta_i = u_i^n - u_i^p + e_{ijk}\left(\omega_j^n r_k^n - \omega_j^p r_k^p\right), \tag{1}$$

where $u_i$ = particle displacement; $\omega_j$ = particle rotation; $r_k$ = vector joining the particle centroid to the contact point; superscripts refer

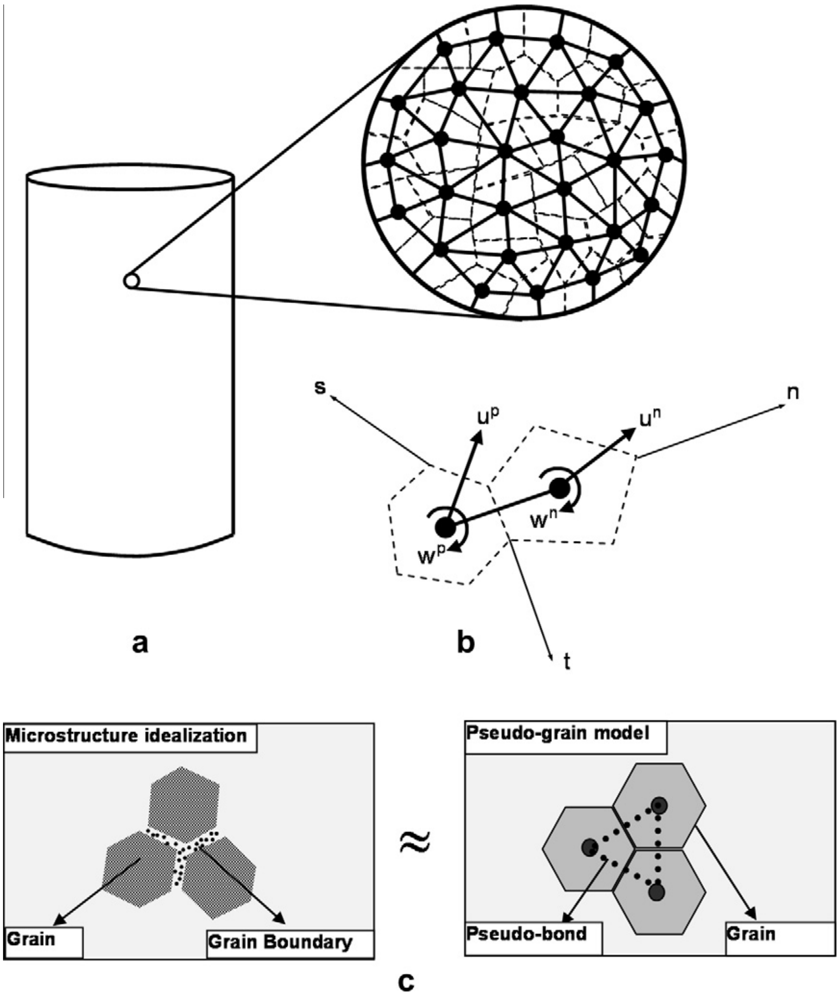

**Fig. 1.** Conceptual granular model of a continuum (a) pseudo-granular structure, (b) two-grain kinematics, and (c) idealization of grain interactions.

to the interacting particles and $e_{ijk}$ = permutation symbol. The relative displacement $\delta_i$ between two grains may be decomposed into two components, one along the pseudo-bond connecting the conceptual grains denoted by, $\delta_n$, and the other in the tangential direction of the pseudo-bond denoted by, $\delta_W$. The relative displacement in the normal direction is given by, $\delta_n = \delta_i n_i$, and the relative displacement in the tangential direction is given by, $\delta_W = \sqrt{(\delta_i s_i)^2 + (\delta_i t_i)^2}$, where the vector $n_i$ = unit vector along the line connecting the grain centroids; and *nst* forms a local Cartesian coordinate system as shown in Fig. 1, where the vectors $s_i$ and $t_i$ are arbitrarily chosen and lie on the plane perpendicular to the vector $n_i$. Thus, upon an increment of deformation, the center-to-center distance between two granular material points, denoted by $L$, becomes, $L_o + \ \delta_n$, where, $L_o$ is the initial center-to-center distance, and the tangential distortion between the two granular material points, denoted by $w$, becomes, $\delta_W$.

The conceptual granular interactions between materials points through pseudo-bond may be expressed as potential function, $\Phi(L,w)$, formulated in terms of the center-to-center distance, $L$, and the tangential distortion, $w$ (Misra et al., 2003), although, more strictly, the particle potential should incorporate the effect of the neighboring grains. Decomposition of energy in terms of dilatational and deviatoric deformation has also been considered by Volokh and Gao (2005) in the context of modified VIB model. For simplicity, the potential function is written as a summation of a central potential, $\phi(L)$, dependent upon the center-to-center distance of two nearest neighbor grains, $L$, and a non-central potential, $\psi(w)$, dependent upon the tangential distortion from the initial equilibrium position for the two nearest neighbor grains, $w$, given by

$$\Phi(L,w,p) = \phi(L,p_L) + \psi(w,p_w), \tag{2}$$

where we have neglected the term that cross-links central and non-central motions and $p = \{p_L, p_w\}$ are a set of parameters, including grain size and shape, that define the potential function. Although the potential functions are inspired by the atomic-interaction potentials, the pseudo-bond potential functions represent the interaction of grains. The grains can be assumed to be formed of domains demarcated by natural grain boundaries as depicted in Fig. 1(c). Thus the grains may be considered as atom aggregations, such that the inter-granular potential may be viewed in a statistical sense as representing the behavior of many interacting atoms comprising the grains. In principle, the inter-granular potentials can be derived in a manner analogous to that of molecular potential energy functions (Murrell et al., 1984). However such an approach is untenable for large grains with billions of atoms.

From an empirical viewpoint, we can formulate functions in which the essential sub-granular scale mechanisms are represented. The parameters of these functions can then be obtained by fitting with experimental data. In the spirit of this more practical approach, we consider the interaction of two grains. Fig. 2(a) gives a schematic plot of the typical shape of pseudo-bond central potential function, $\phi(L)$. When the grains are pulled apart along the centroidal axis, the pseudo-bond central potential, $\phi(L)$, can be expected to decay asymptotically to zero starting from some equilibrium value. Phenomenologically, the decay represents an accumulation of damage caused by sub-granular scale de-cohesion and void growth (Misra et al., 2007). Similarly, when the grains are compressed against each other and the center-to-center distance is decreased; the pseudo-bond potential function is expected to account for the effects of damage due to sub-granular scale shear localization or void collapse. Possible mechanism of inter-granular compressibility in the context of cohesive materials, such as cements and rocks has been discussed by van Mier (2007). The potential function under grain compression is expected to be considerably softer and less rapidly varying than the atomic potentials which rapidly approach infinity as the center-to-center distance is decreased. Inter-particle or polyatomic potential functions are known to be less steep on the compressive (or repulsive) side compared to their inter-atomic counterparts (Murrell et al., 1984; Israelachvili, 1985). The force resultant from the relative movement between two adjacent grains can then be obtained as the derivatives of the inter-granular potential functions. For convenience, we directly formulate the force functions, which are given as follows for the force generated by the relative normal motions of the adjacent grains:

$$f_n = A\delta_{\mathrm{n}} e^{-\left(\frac{\delta_{\mathrm{n}}}{B}\right)} \quad \text{for tension}, \tag{3}$$

$$f_n = A\delta_{\mathrm{n}} - \frac{A}{2\alpha_1} \ln[(1 - \tanh\alpha_1\delta_{\mathrm{n}})(1 + \tanh\alpha_1\delta_{\mathrm{n}})] \quad \text{for compression}. \tag{4}$$

Eq. (3) represents a characteristic damage behavior based upon the attractive part of the well-known Morse potential function and has been used previously to represent inter-granular damage (de-cohesion) under tension (Gao and Klein, 1998). Under compression, the inter-granular force function can take a variety of forms depending upon the sub-granular structure and composition. For instance, under purely central compression of two-grains, the sub-granular scale pore compaction or shear localization can result in the force function reaching an asymptotic value, as opposed to infinitely increasing. Eq. (4) is a hyperbolic force function formulated to approach an asymptotic value as the inter-granular center-to-center distance is decreased. Other formulations of force function under grain compression are possible and need further investigation. Fig. 3(a) plots the above force functions with respect to the normal component of the inter-granular relative displacement.

Similarly sub-granular scale mechanisms need to be accounted when the grains are deformed in the direction tangential to the pseudo-bond. For example, greater energy may be required to ini-

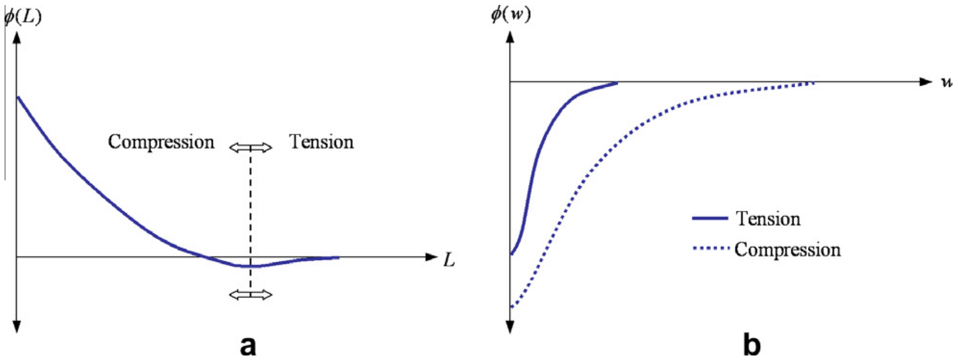

**Fig. 2.** Pseudo-potential functions in (a) normal direction and (b) tangential direction.

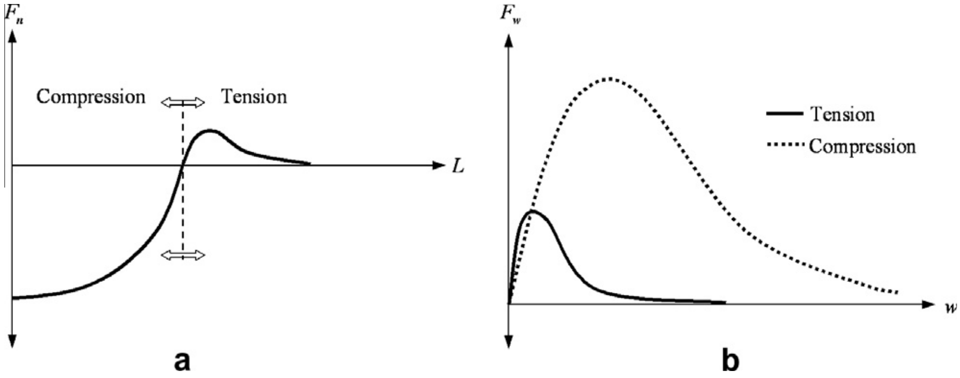

**Fig. 3.** Force functions in (a) normal direction and (b) tangential direction.

tiate damage in the direction tangential to the pseudo-bond under compression in contrast to that under tension. Such phenomena may be caused by the differences in interactions at the grain boundaries under tensile or compressive conditions. The analysis of inter-granular behavior undergoing damage in the presence of many sub-granular scale fractures and flaws at the grain boundaries under combined normal and shear loading is highly complex. However, the indications for the differences in the inter-granular shear behavior under different normal loading conditions are available from the pressure dependent behavior shown by single fractures subjected to shear (Misra, 2002). Hence, under compression; a deeper potential-well is expected for the non-central potential, $\phi(w)$. The pseudo-bond potential functions have to be formulated accordingly. Fig. 2(b) gives a schematic plot of the shapes of possible non-central bond potential functions, $\phi(w)$, for the case of grains under tension or compression. It is reasonable to assume that the non-central potential functions resemble the tensile part of the inter-granular central potential in which the energy associated with the interaction decay asymptotically to zero with increasing tangential distortion starting from some equilibrium value. In Fig. 2, the point of lowest potential corresponds to the equilibrium center-to-center distance, $L = L_o$ and the equilibrium tangential distortion, $w = 0$. Again for convenience, we directly formulate the force functions, which are given as follows for the force generated by the relative tangential motions of the adjacent grains:

$$f_w = C\delta_\mathrm{w} e^{-\left(\frac{\delta_\mathrm{w}}{D}\right)} \quad \text{for tension}, \tag{5}$$

$$f_w = C\delta_\mathrm{w} e^{-\left(\frac{\delta_\mathrm{w}}{\alpha_2 D}\right)} \quad \text{for compression}. \tag{6}$$

For simplicity, Eqs. (5) and (6) are taken to have the same form as Eq. (3). In addition, as a first step to account for the effect of normal loading, the force functions are modified to have different parameters under tension and compression. Modifications to these force functions, that incorporate normal force dependency, such as a frictional law, may also be considered and need further investigations. These force functions exhibit the non-linear pre-peak and softening response that can be expected for grain boundaries experiencing damage under shear loading. Fig. 3(b) plots the above force functions with respect to the tangential component of the inter-granular relative displacement.

Based upon the above force functions, the incremental inter-granular force $\Delta f_i$ may be related to the increment of relative displacement $\Delta\delta_j$ through the stiffness $K_{ij}$ as

$$\Delta f_i = K_{ij}\Delta\delta_j, \tag{7}$$

where the stiffness $K_{ij}$ can be written in terms of the components in the normal direction $K_n$ and the tangential direction $K_w$ as

$$K_{ij} = K_n n_i n_j + K_w(s_i s_j + t_i t_j). \tag{8}$$

The stiffness in the normal direction $K_n$ and that in the tangential direction $K_w$ are obtained from the force functions in Eqs. (3)–(6) as follows:

$$K_n = \frac{\partial f_n}{\partial L} = -\frac{A e^{-\left(\frac{\delta_\mathrm{n}}{B}\right)}(-B + \delta_\mathrm{n})}{B} \quad \text{for tension}. \tag{9}$$

$$K_n = \frac{\partial f_n}{\partial L} = A[1 + \tanh(\alpha_1\delta_\mathrm{n})] \quad \text{for compression}. \tag{10}$$

$$K_w = \frac{\partial f_w}{\partial w} = \frac{C e^{-\left(\frac{\delta_\mathrm{w}}{D}\right)}(D - \delta_\mathrm{w})}{D} \quad \text{for tension}. \tag{11}$$

$$K_w = \frac{\partial f_w}{\partial w} = \frac{C e^{-\left(\frac{\delta_\mathrm{w}}{\alpha_2 D}\right)}(\alpha_2 D - \delta_\mathrm{w})}{\alpha_2 D} \quad \text{for compression}. \tag{12}$$

Fig. 4 presents these stiffnesses with respect to the relative displacements in the normal and tangential directions, respectively. We note the force functions under tension and compression are formulated in a way that the stiffness is same under initial zero-strain condition ($\delta_n = 0$, $\delta_w = 0$).

## 3. Constitutive relationship for idealized granular system

The incremental stress tensor of an element of a granular medium containing a number of grains may be expressed as a volume average of the tensor product of the incremental inter-granular force, $\Delta f_i$, and the vector joining the contacting grain centroid, $L^p n_j^p$, given as (Chang and Liao, 1994):

$$\Delta\sigma_{ij} = \frac{1}{V}\sum_p L^p \Delta f_i^p n_j^p, \tag{13}$$

where the summation is performed over all the inter-granular interactions within the representative volume, $V$. We now utilize a kinematical assumption that relates the relative displacement between grains, $\Delta\delta_i$, and the overall strain of the sample, $\Delta\varepsilon_{ij}$, as follows (Chang et al., 2002)

$$\Delta\delta_i = L\Delta\varepsilon_{ij} n_j, \tag{14}$$

where the strain, $\Delta\varepsilon_{ij}$, is treated as symmetric, given as

$$\Delta\varepsilon_{ij} = \frac{1}{2}(u_{i,j} + u_{j,i}) \tag{15}$$

and as a first approximation, we ignore the micro-polar effects introduced by grain rotations. The constitutive tensor of the sample is obtained by combining the inter-granular force–displacement relationship from Eq. (7) with Eqs. (13) and (14) as follows:

$$C_{ijkl} = \frac{1}{V}\sum\nolimits_p L^{p^2} n_j^p n_l^p K_{ik}^p, \tag{16}$$

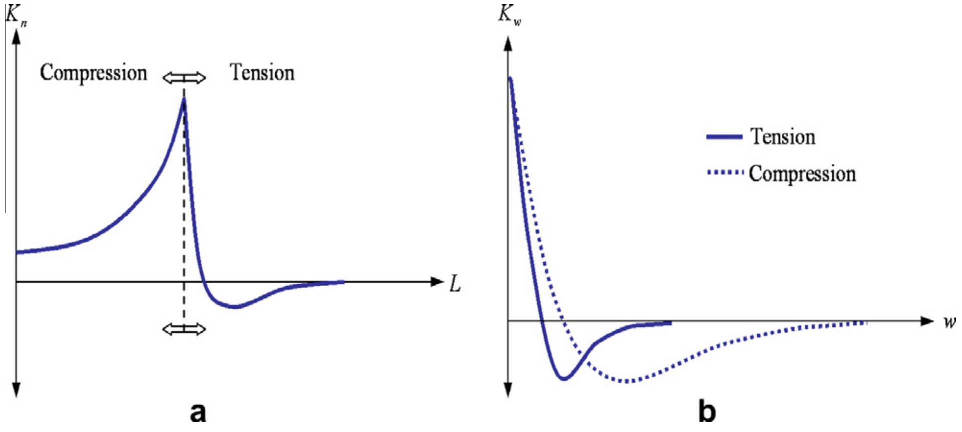

**Fig. 4.** Stiffness functions in (a) normal direction and (b) tangential direction.

where the relationship between the incremental stress $\Delta\sigma_{ij}$ and incremental strain $\Delta\varepsilon_{ij}$ is expressed as

$$\Delta\sigma_{ij} = C_{ijkl}\Delta\varepsilon_{kl}, \tag{17}$$

For a representative volume containing a large number of grains, the summation in Eqs. (13) and (16) may be recast into an integral form as follows (Chang and Misra, 1990)

$$\Delta\sigma_{ij} = LN_p \int_\Omega n_i(\Omega)\Delta f_j(\Omega)\xi(\Omega)d\Omega, \tag{18}$$

$$C_{ijkl} = L^2N_p \int_\Omega n_j(\Omega)K_{ik}(\Omega)n_l(\Omega)\xi(\Omega)d\Omega, \tag{19}$$

where the integration $\int_\Omega ()d\Omega = \int_0^{2\pi}\int_0^{\pi}()\sin\gamma d\gamma d\beta$. In this integration,$\gamma$ is taken as the polar angle (colatitudinal) from the positive z-axis with $\gamma$ $[0,\pi]$, and $\beta$ is the azimuthal angle (longitudinal) in the x–y plane from the *x*-axis with $\beta$ $[0,2\pi]$. In Eqs. (18) and (19), $N_p$ is the pseudo-bond density, namely the inter-granular interaction density, per unit volume and $\xi(\Omega)$ is a directional density function which represents the discrete distribution of inter-granular interactions in a continuum manner, such that the product $N_p$ $\xi(\Omega)$ $d\Omega$ denotes the inter-granular interaction density in the direction represented by the interval between solid angles $\Omega$ and $\Omega + d\Omega$. In three dimensions, spherical harmonic expansions may be utilized as the directional density function as discussed in Chang and Misra (1990). For the simplicity of further derivation, a truncated form of spherical harmonic expansion is employed and given as

$$\xi(\gamma,\beta) = \frac{1}{4\pi}\left[1 + \frac{1}{4}a_{20}(3\cos 2\gamma + 1) + 3\sin^2\gamma(a_{22}\cos 2\beta + b_{22}\sin 2\beta)\right] \tag{20}$$

where $a_{20}$, $a_{22}$ and $b_{22}$ are fabric parameters determining the isotropy of the material. For instance, if $a_{20} = a_{22} = b_{22} = 0$, then the truncated distribution density function is capable of representing material having isotropic symmetry. The material will have transverse isotropic symmetry when the fabric parameters $a_{22} = b_{22} = 0$. If we choose the fabric parameters such that $a_{20} \neq a_{22} \neq 0$ then it represents material with orthotropic symmetry.

## 4. Results and discussion

### 4.1. Closed form expression for initial moduli

Since, in general the force and stiffness functions depend upon orientations, closed form integration of Eqs. (18) and (19) may only be obtained under certain simple loading conditions or under infinitesimally small strains in which case the stiffnesses, $K_n$ and $K_w$, reduce to constant values. Substituting Eq. (8), the stiffness functions, $K_{ij}$, and Eq. (20), the directional density function of the pseudo-bonds, into Eq. (19), closed form solutions for the initial moduli of the sample may be derived. Taking into account the symmetry of the incremental stress and strain tensors, the stress–strain relationship, equivalent to Eq. (17), can be re-expressed in Voigt's notation as follows:

$$\Delta\sigma_m = C_{mn}\Delta\varepsilon_n, \tag{21}$$

or

$$\begin{bmatrix} \Delta\sigma_{zz} \\ \Delta\sigma_{yy} \\ \Delta\sigma_{xx} \\ \Delta\sigma_{zy} \\ \Delta\sigma_{zx} \\ \Delta\sigma_{xy} \end{bmatrix} = \begin{bmatrix} C_{11} & C_{12} & C_{13} & 0 & 0 & C_{16} \\ & C_{22} & C_{23} & 0 & 0 & C_{26} \\ & & C_{33} & 0 & 0 & C_{36} \\ & & & C_{44} & C_{45} & 0 \\ & \text{Symmetric} & & & C_{55} & 0 \\ & & & & & C_{66} \end{bmatrix} \begin{bmatrix} \Delta\varepsilon_{zz} \\ \Delta\varepsilon_{yy} \\ \Delta\varepsilon_{xx} \\ \Delta\varepsilon_{zy} \\ \Delta\varepsilon_{zx} \\ \Delta\varepsilon_{xy}, \end{bmatrix} \tag{22}$$

The initial moduli, $C_{mn}$, are given as

$$C_{11} = L_o^2N_p\left[\frac{1}{15}(3K_n + 2K_w) + \frac{a_{20}}{105}(12K_n + 2K_w)\right], \tag{23}$$

$$C_{12} = L_o^2N_p\left[\frac{1}{15}(K_n - K_w) + \frac{a_{20}}{105}(K_n - K_w) + \frac{a_{22}}{35}(2K_n - 2K_w)\right], \tag{24}$$

$$C_{13} = L_o^2N_p\left[\frac{1}{15}(K_n - K_w) + \frac{a_{20}}{105}(K_n - K_w) + \frac{a_{22}}{35}(-2K_n + 2K_w)\right], \tag{25}$$

$$C_{16} = L_o^2N_p\left[\frac{b_{22}}{35}(2K_n - 2K_w)\right], \tag{26}$$

$$C_{22} = L_o^2N_p\left[\frac{1}{15}(3K_n + 2K_w) + \frac{a_{20}}{105}(-6K_n - K_w) + \frac{a_{22}}{35}(12K_n + 2K_w)\right], \tag{27}$$

$$C_{23} = L_o^2N_p\left[\frac{1}{15}(K_n - K_w) + \frac{a_{20}}{105}(-2K_n + 2K_w)\right], \tag{28}$$

$$C_{26} = L_o^2N_p\left[\frac{b_{22}}{35}(6K_n - 6K_w)\right], \tag{29}$$

$$C_{33} = L_o^2N_p\left[\frac{1}{15}(3K_n + 2K_w) + \frac{a_{20}}{105}(-6K_n - K_w) + \frac{a_{22}}{35}(-12K_n - 2K_w)\right], \tag{30}$$

$$C_{36} = L_o^2N_p\left[\frac{b_{22}}{35}(6K_n + 8K_w)\right], \tag{31}$$

$$C_{44} = L_o^2 N_p \left[ \frac{1}{15}(K_n + 4K_w) + \frac{a_{20}}{105}(K_n + 13K_w) + \frac{a_{22}}{35}(2K_n - 2K_w) \right], \tag{32}$$

$$C_{45} = L_o^2 N_p \left[ \frac{b_{22}}{35}(2K_n - 2K_w) \right], \tag{33}$$

$$C_{55} = L_o^2 N_p \left[ \frac{1}{15}(K_n + 4K_w) + \frac{a_{20}}{105}(K_n + 13K_w) + \frac{a_{22}}{35}(-2K_n + 2K_w) \right], \tag{34}$$

$$C_{66} = L_o^2 N_p \left[ \frac{1}{15}(K_n + 4K_w) + \frac{a_{20}}{105}(-2K_n - 5K_w) + \frac{a_{22}}{5}(2K_w) \right]. \tag{35}$$

The other elements of the constitutive relation, $C_{mn}$, are all zero. By using the above derived constitutive relations and appropriate bond density parameters, $a_{20}$, $a_{22}$, and $b_{22}$, which are the indications of the type of material symmetry, material properties such as Young's modulus, $E$, Poisson's ratio, $v$, and shear modulus, $G$, in different directions corresponding to those bond density parameters may be obtained. As an example, we derive the material properties for isotropic material whose bond density parameters, $a_{20} = a_{22} = b_{22} = 0$. Further, under infinitesimal initial strain, both $\delta_n \to 0$ and $\delta_w \to 0$, and Eqs. (9)–(11) reduce to $K_n = A$ and $K_w = C$. Thus, the initial Young's modulus, $E$, and Poisson's ratio, $v$, fo an isotropic material are obtained as

$$E = L_o^2 N_p \frac{A(2A + 3C)}{3(4A + C)}, \tag{36}$$

$$v = \frac{A - C}{4A + C}. \tag{37}$$

For positive values of parameters $A$ and $C$, Eq. (37) predicts a Poisson's ratio in the range of −1–0.25, which conforms to the well-known bounds for isotropic elastic materials. For most bulk cohesive materials, Poisson's ratio is positive, however, auxetic cohesive materials with negative Poisson's ratios are possible as well. By applying similar operations, material properties for various types of materials such as transversely isotropic and orthotropic material etc. can be expressed in terms of normal and tangential force laws as well as bond density parameters.

### *4.2. Model parameters*

There are six model parameters that determine the force–displacement functions and stiffness functions, namely $A$, $B$, $C$, $D$, $\alpha_1$ and $\alpha_2$. In addition, there are two micro-structural parameters given in terms of the bond length, $L_0$, and the number of bonds per unit volume (bond density), $N_p$. The determination of these parameters is imperative in order to subsequently calculate the stress–strain relationships of a material. Parameters $A$, $B$ and $\alpha_1$ determine the normal inter-granular force functions, and $C$, $D$ and $\alpha_2$ determine the tangential inter-granular force functions. Parameter $A$, is the normal stiffness at the zero-strain condition; parameter $B$, defines the deformation corresponding to the peak tensile force; and parameter $\alpha_1$ determines the deformation corresponding to the maximum curvature of the compressive force–deformation curve. Similarly, parameter $C$, is the shear stiffness at the zero-strain condition; parameter $D$, defines the deformation corresponding to the peak tangential force; and parameter $\alpha_2$ modifies the deformation corresponding to the peak tangential force when the grains are under the compression. These parameters are related to the grain characteristics, including its size, composition, and sub-granular structure. Ideally, the model parameters may be obtained by averaging over the configurational space of grain microscopic constituents simulated using appropriate methods, such as particle or atomistic simulation approaches. Alternatively, these parameters can be correlated to the grain-scale characteristics, by fitting to measured properties obtained from physical experiments for materials whose constituent properties are known.

A systematic parametric study may be conducted to obtain the admissible ranges of force-law and bond density parameters. For an isotropic material, parameters $A$ and $C$ may be derived from measured Young's modulus and Poisson's ratio as follows using Eqs. (36) and (37):

$$A = \frac{3E}{(1 - 2v)L_o^2 N_P}, \tag{38}$$

$$C = \frac{3E(1 - 4v)}{(1 - 2v)(v + 1)L_o^2 N_P}. \tag{39}$$

For the pseudo-bond model, the product $L_0^2 N_p$ can be conveniently incorporated into modified parameters denoted by, $A_1$ and $C_1$, as follows:

$$A_1 = A L_o^2 N_P, \tag{40}$$

$$C_1 = C L_o^2 N_P. \tag{41}$$

The relationships of parameters $A_1$ and $C_1$ with positive Poisson's ratio for three values of Young's modulus E are plotted in Fig. 5(a) and (b), respectively. Clearly, we do not need to explicitly know the numerical values of either the bond length or the bond density for performing model calculations. On the other hand, if the micro-scale length parameters and bond density can be identified from the experimental measurements of material constituents, the intrinsic model parameters with clear physical meaning can be obtained.

The other model parameters, $B$, $D$, $\alpha_1$, and $\alpha_2$, can be numerically obtained by considering the measured peak state of stress–strain curve under the uniaxial tensile and compressive loading. Parameters $B$ and $D$ are closely related to the peak stress and corresponding strain measured in a uniaxial tension test. Similarly, parameter $\alpha_1$ and $\alpha_2$ have a close relationship to the failure stress and the corresponding strain in a uniaxial compression test. To determine the

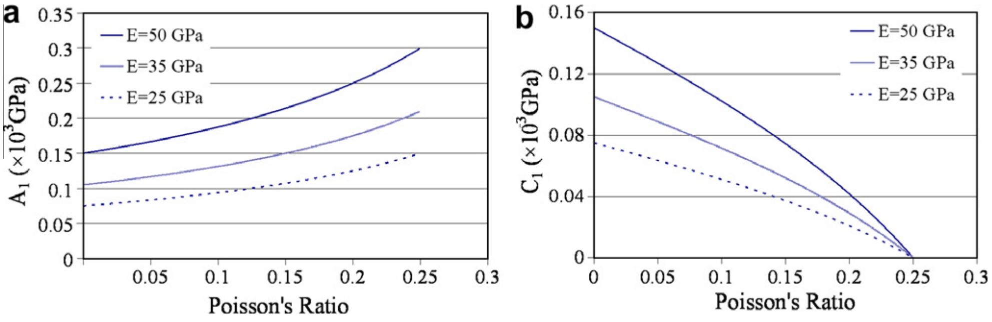

**Fig. 5.** (a) Parameter A$_1$ vs Poisson's Ratio (b) Parameter C$_1$ vs Poisson's Ratio.

feasible range of these parameters, a parametric study maybe performed by varying one of the parameter while keeping the others constant. In Fig. 6, we show example results of a parametric study performed by varying parameters $B$ and $D$. Based upon these parametric studies, charts (such as Fig. 6(b)) can be developed that relate the parameters to the peak/failure stress and strain of uniaxial tension and compression tests.

### *4.3. Stress–strain behavior under multi-axial loading conditions*

To evaluate the model capability, we present selected results for stress–strain behavior under monotonic uniaxial, biaxial and triaxial tension and compression and compare them with available experimental measurements. For these loading conditions, the stress–strain relationship is obtained by numerically integrating Eq. (17) or Eq. (18) to obtain the incremental stresses $\Delta\sigma_{ij}$ or the incremental strains $\Delta\varepsilon_{ij}$ or their combination under the applied loading conditions.

#### *4.3.1. Uniaxial tension and compression*

For simulating uniaxial stress test, we specify axial strain increments $\Delta\varepsilon_{11} \neq 0$ and the non-axial components of stress increments $\Delta\sigma_{ij} = 0$ and we compute the axial stress increments $\Delta\sigma_{11}$ and the non-axial components of strain increments $\Delta\varepsilon_{ij}$. For our example calculations, we have used the following values of the model parameters: $A_1 = 0.7$, $B = 3.4 \times 10^{-7}$, $C_1 = 0.2$, $D = 1.3 \times 10^{-4}$, $\alpha_1 = 2 \times 10^5$ and $\alpha_2 = 7$. These parameters were calculated to fit the measured uniaxial tension stress–strain curve for portland cement concrete plate (Gopalaratnam and Shah, 1985). Fig. 7 shows the measured and calculated stress–strain curve under uniaxial tension. The measured data, shown by symbols, was obtained from uniaxial tension test done with symmetrically notched plates (Gopalaratnam and Shah, 1985). The strain measurements were made using 10 mm long strain gages mounted along the centerline joining the notches. The calculated stress–strain curve using the derived model, shown as solid line in Fig. 7, provides an excellent match to the measured data indicating the models ability to replicate the behavior. The measured strains were also obtained from the overall displacement of the sample over a gage length of 83 mm. Gopalaratnam and Shah (1985) found that the strains measured by the 10 mm long strain gage increased rapidly in the post peak in contrast to the strain obtained from the overall displacements. This phenomenon is attributed to the strain localization along the centerline joining the notches during the post peak regime accompanied by unloading in regions away from the localization zones.

Fig. 8, plots the stress–strain relationship under uniaxial compressive loading obtained from the calculation. Although there is no experimental observation for the same material tested under uniaxial compression, the curve exhibits a reasonable result as the stress and strain at the peak condition are approximately ten times higher than that under tensile loading which is widely observed for this type of cementitious materials.

#### *4.3.2. Biaxial tension and compression*

In Figs. 9 and 10 we compare the predicted stress–strain curves with the measured data for two sets of biaxial tests. The measured

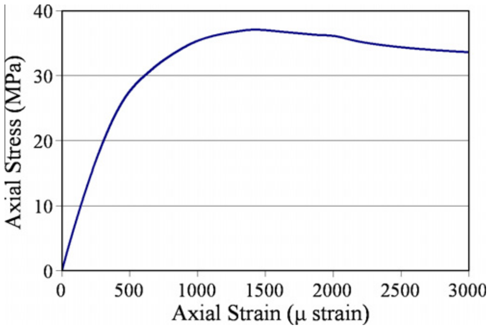

**Fig. 8.** Predicted stress–strain behavior under uniaxial compression.

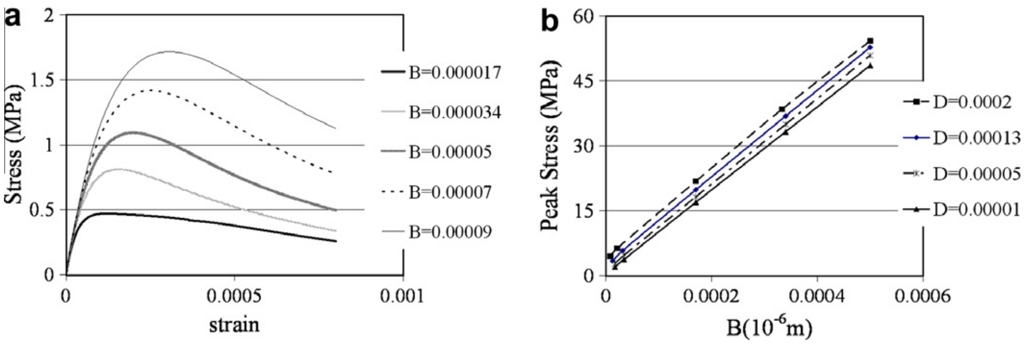

**Fig. 6.** (a) Uniaxial tension stress–strain curves obtained by varying parameter B while the other parameters are kept constant (b) peak stress vs parameter B for different values of parameter D obtained for stress–strain curves similar to (a).

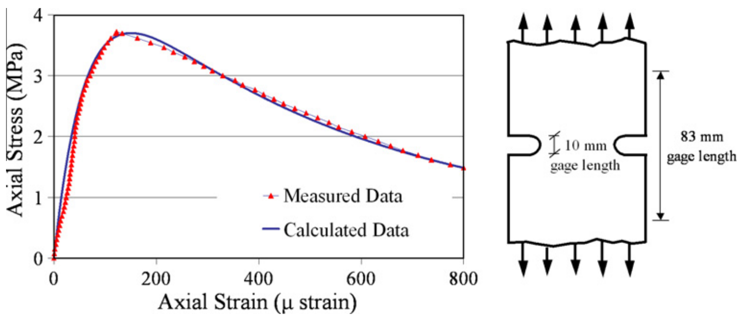

**Fig. 7.** Measured (Gopalaratnam and Shah, 1985) and calculated stress–strain curve under uniaxial tension.

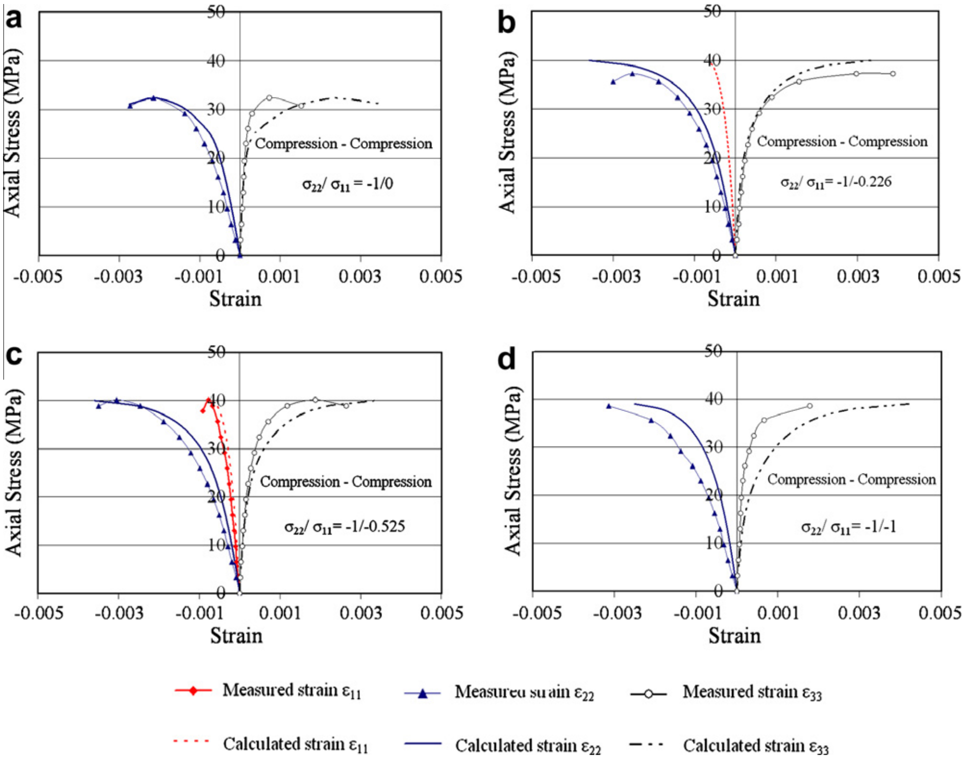

**Fig. 9.** Measured (Kupfer, 1973 as reported by van Mier, 1997) and calculated stress–strain curves under biaxial loading path.

data are also for portland cement concrete plates although these are from experiments performed by different researchers (Kupfer, 1973 as reported by van Mier, 1997; Yin et al., 1989) and represent concrete samples whose mix proportions (compositions) are also different. Nevertheless, we have used the same model parameters as those used for uniaxial test calculation in order to assess if the model predictions capture the behavior exhibited by these materials. For simulating these tests we specify stress increments $\Delta\sigma_{ij}$

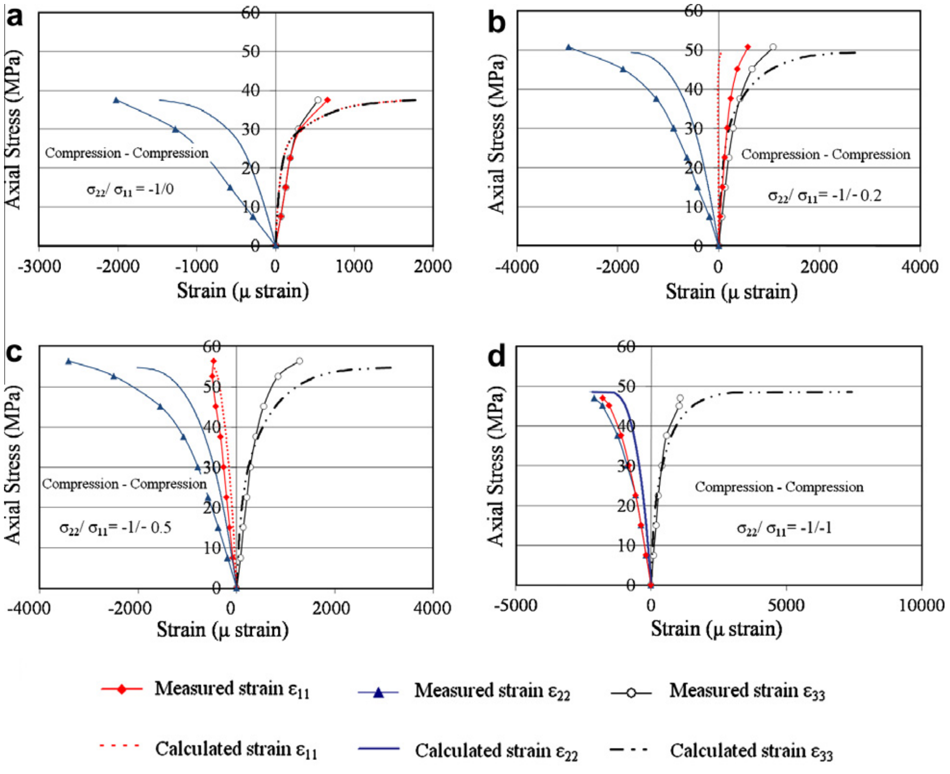

**Fig. 10.** Measured (Yin et al., 1989) and calculated stress–strain curves under biaxial loading path.

such that the ratio $\sigma_{22}/\sigma_{11}$ = constant and $\sigma_{33} = 0$, and we compute the strain increments $\Delta\varepsilon_{ij}$. In both Figs. 9 and 10, the four biaxial test measurements are for the condition in which the non-zero stresses, $\sigma_{11}$ and $\sigma_{22}$, are under compression. The stress–strain curves are shown by plotting the largest normal stress, typically $\sigma_{22}$, denoted as the "axial stress" against all the normal strain components. In Fig. 9(a) and Fig. 10(a), since the stress component $\sigma_{11} = 0$, the stress condition is uniaxial, consequently the strain components $\varepsilon_{11} = \varepsilon_{33}$. In Fig. 9(b) and (c), and Fig. 10(b) and (c), the three normal strain components are distinct. In Fig. 9(d) and Fig. 10(d), since the stress component $\sigma_{11} = \sigma_{22}$, the strain components $\varepsilon_{22} = \varepsilon_{11}$. The predicted data shown in Figs. 9 and 10 replicate the observed trends reasonably well and in some cases show close quantitative agreement. These predictions are rather encouraging since we have used the same model parameters in our calculations although the mix proportions for both these data sets are different from those used by Gopalaratnam and Shah (1985). Clearly closer quantitative agreement between measured stress–strain curves and predictions can be obtained by adjusting the model parameters. We have further compared the predicted failure behavior under these biaxial loading paths with that obtained from the measurements. Failure is identified from the predicted stress–strain curves in a manner identical to that for experimentally measured stress–strain curves at either the peak or asymptotic major principal stress value. As seen from Fig. 11, the predicted failure behavior not only matches the measured data by Yin et al. (1989) but replicates the biaxial failure envelope shape widely reported in the literature for concrete and hardened cement paste.

### 4.3.3. Triaxial tension and compression

In Figs. 12–14 we show the stress–strain behavior predicted by the derived constitutive relationships under various triaxial tension and compression loading paths. Figs. 12 and 13 give the stress–strain and volume change behavior under axisymmetric triaxial loading path in which a compressive constant confining stress given by $\sigma_{22} = \sigma_{33}$ = constant is applied while the axial stress, $\sigma_{11}$,

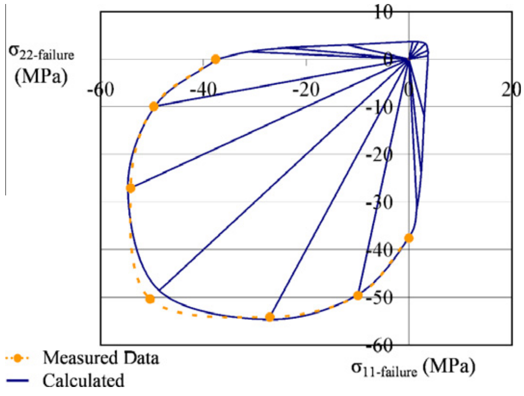

**Fig. 11.** Calculated failure envelope under biaxial loading for $\sigma_{33} = 0$ showing comparison with measured data (Yin et al., 1989).

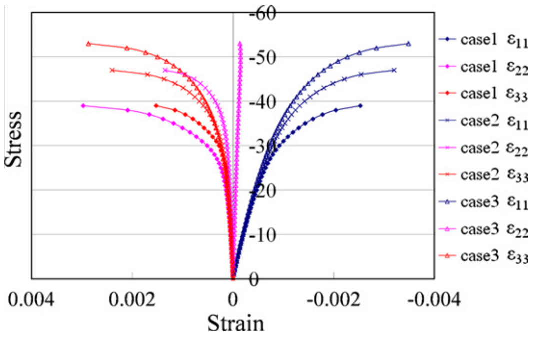

**Fig. 14.** Predicted stress–strain curves under true triaxial loading that replicate the test conditions reported by van Mier (1984) for tests on concrete cubes.

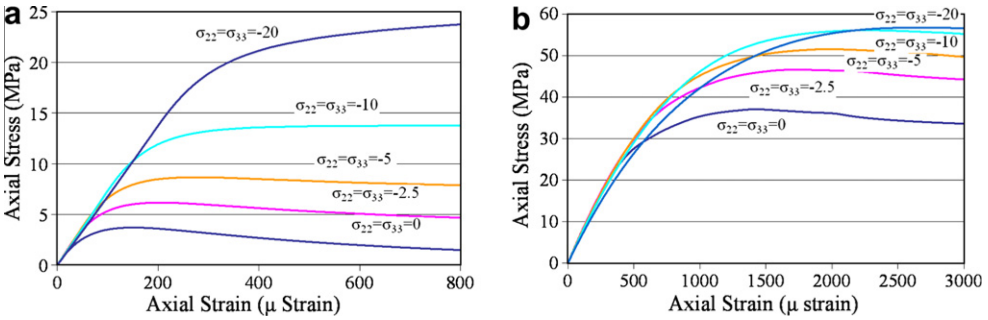

**Fig. 12.** Axisymmetric triaxial stress–strain relationship for (a) tension and (b) compression.

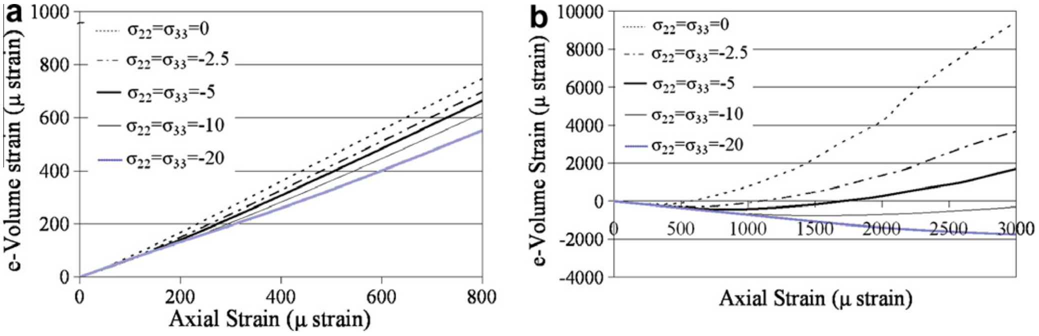

**Fig. 13.** Axisymmetric triaxial volumetric strain relationship for (a) tension and (b) compression.

is increased either in tension or in compression. Clearly, the confining stress has a significant effect upon the stress–strain and volume change behavior under tension as well as under compression. Both the failure stress and the corresponding strain increase with increasing confining pressures. Similar behavior has been observed in experiments on concrete samples subjected to triaxial compression (Xie et al., 1995; Balmer, 1949). The volume change predictions show that under tension the behavior is always dilative, while under compression, the volume compresses and, subsequently dilates. Such volume change behavior is suspected for all brittle cohesive materials, although experimental measurements are not always widely available.

For the case of tensile loading, the failure is primarily governed by a combination of two mechanisms: (1) inter-granular failure in the normal direction under tension described by Eq. (3) and (2) inter-granular failure in the shear direction under compression described by Eq. (6). The other two mechanisms described by Eqs. (4) and (5), have a smaller contribution under this type of loading condition. As the axial tensile stress is increased, the inter-granular orientations that reach peak tensile force under tension have to first overcome the compressive forces induced by the confining stress. In addition, the inter-granular orientations that reach peak shear force do so under a compressive loading condition. For either failure mechanism, the resultant peak force values and inter-granular motion are larger under greater confinement. Furthermore, for tensile axial loading, the dilative volume change behavior shown in Fig. 13(a) indicates that the failure is dominated by the normal tensile mechanism, although, the reduced volume dilation indicates that the deformation and failure have increasing contribution from the shear mechanism under increasing confinement. For the case of compressive loading, the failure is governed by a combination of all four inter-granular interaction mechanisms. Under uniaxial compressive stress ($\sigma_{22} = \sigma_{33} = 0$), the normal tensile mechanism has the greatest contribution as indicated by the dilative volume change behavior shown in Fig. 13(b). As the confining stress in increased, the shear mechanisms become important. Finally, at very high confining stresses, the inter-granular failure in the normal direction under compression is the dominant mechanism. We also note that there is a relatively large increase in the failure stress and the corresponding strain for the case of tensile loading as opposed to the compressive loading for the same increase in the confining stress. These differences are likely due to the different mechanisms that govern the behavior under the two set of loading conditions. For instance, under tensile loading the normal tensile mechanism dominates in which the compressive forces that need to be overcome are proportional to the applied confining stress.

Furthermore, we note that the stress–strain behavior for both set of loading conditions transitions from "brittle" (characterized by a peak stress and post peak softening) to "ductile" (characterized by gradual yielding and post-yield hardening) with increasing confining stress. Experiments on concrete samples subjected to triaxial compression loading have shown similar brittle to ductile transformation under increasing confinement (Xie et al., 1995; Balmer, 1949). The transition is a manifestation of the change affected by the confining stress on the load–displacement states of the four inter-granular interactions (given by Eqs. (3)–(6)) in different inter-granular orientations. The result is that the contributions of these four mechanisms to the overall behavior at different stages of loading vary with confinement similar to variations in the inter-granular deformation mechanisms observed in nano-indentation simulations (Szlufarska et al., 2005). For instance, as the confining stress is increased for tensile axial loading case, the inter-granular softening response in both normal and shear directions are achieved for fewer and fewer orientations and other stiffer and stronger mechanism have a greater contribution. Thus, the overall response acquires a hardening nature with increasing confinement. The precise contributions of the different mechanisms on the deformation and failure response needs further systematic investigation and will be a subject of future publication.

In Fig. 14, we have plotted the predicted stress–strain behavior under true triaxial loading paths that replicate the test conditions reported by van Mier (1984) for tests on concrete cubes. Three loading paths were considered in which the samples were subjected to compressive loads that were increased such that the principal stress ratios $\sigma_{22}/\sigma_{11}$ and $\sigma_{33}/\sigma_{11}$ remained constant during the test. For case 1 the ratio $\sigma_{22}/\sigma_{11} = 0$, for case 2 the ratio $\sigma_{22}/\sigma_{11} = 0.1$, and for case 3 the ratio $\sigma_{22}/\sigma_{11} = 0.33$. For all the three cases the ratio $\sigma_{33}/\sigma_{11}$ was maintained at 0.05. No attempt was made to obtain a quantitative match and the same set of parameters were used as those for the uniaxial and biaxial predictions, although the concrete mix compositions were likely to be different. The predicted curves captured the trends observed in the measurements.

Finally, we have studied the ability of our model to predict the failure behavior under various triaxial loading conditions. The predicted maximum strength curve under axisymmetric triaxial loading at different confining stresses is shown in Fig. 15 which gives a plot of peak axial stress versus the confining stress normalized by the strength under uniaxial stress conditions. The predicted curve compares well with the data widely reported in the literature for concrete and rocks which are characterized by the nonlinear behavior with increasing confining stress (van Mier, 1997; Jaeger et al., 2007). We have also studied failure behavior under true triaxial stress conditions by performing calculations for loading paths in which $\sigma_{22}\ /\sigma_{11} = \text{constant}$ and $\sigma_{33} = \text{constant}$. The predicted failure behavior is shown in Fig. 16, which plots the failure enve-

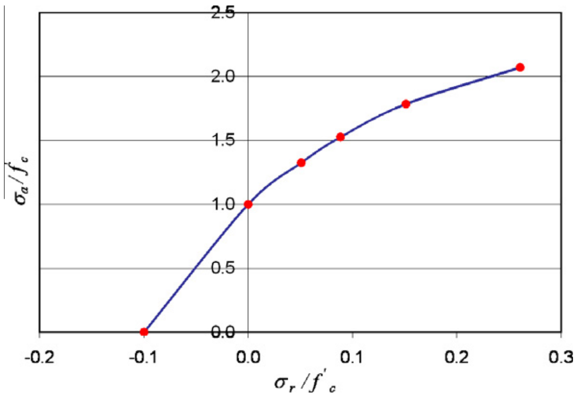

**Fig. 15.** Predicted maximum strength curves under axisymmetric triaxial loading paths ($\sigma_a$=axial stress, $\sigma_r$=confining stress, $f'_c$=uniaxial compressive strength).

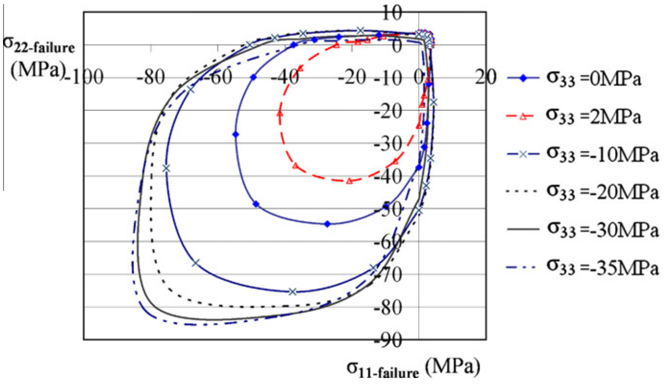

**Fig. 16.** Predicted failure envelopes under true triaxial loading calculated for varying $\boldsymbol{\sigma}_{33}$.

lopes for various values of $\sigma_{33}$, as the material is subjected to a $\sigma_{22}/\sigma_{11}$ = constant stress-path. As the stress $\sigma_{33}$ is increased from a tensile value of 2 MPa to a compressive value of $-35$ MPa, the failure envelope progressively becomes larger. We note that the failure envelopes for compressive stresses $-30$ and $-35$ MPa are almost coincident indicating that the material is close to its triaxial compressive strength limit.

## 5. Summary and conclusion

We have presented a methodology for obtaining the constitutive relationships for cohesive materials based upon a microstructural mechanics approach used in granular mechanics. The stress–strain relationships were derived by considering the material to be composed of grains, whose interactions are governed by force–displacement relations inspired by the atomistic-level particle interactions. We find that the microstructural granular mechanics approach is versatile and can be applied to granular assemblies with diverse inter-granular behavior. Since these inter-granular pseudo-bonds considered here model the behavior of collection of atoms, the force-laws that describe their behavior were crafted in a manner that captures the effect of sub-granular damage for both the normal and tangential interactions. The overall constitutive law of the material was then obtained by averaging over the random network formed by the pseudo-bonds.

The developed methodology was used to derive closed form of stress–strain relationships under initial infinitesimal load. The closed form relationships provide us with a means to relate two of the six model parameters to the measured elastic behavior of cohesive materials. The other four model parameters can be calibrated to the measured peak stress and corresponding strain from uniaxial tension and compression tests. Further research is necessary to obtain feasible range of parameters for different cohesive material systems. The model applicability was then evaluated by comparison of the calculated stress–strain relations as well as the failure behavior to the available experimental data under uniaxial, biaxial and triaxial loading conditions. We found that when uniaxial test data was available for parameter calibration, the model provided an excellent prediction of the overall behavior under multi-axial loading paths. From the variety of comparisons between predicted results and experimental observations, we can conclude that the model is able to capture several stress–strain phenomena under various loading conditions. The model versatility can be attributed to the interaction of inter-granular behavior in various orientations that provide competing deformation mechanisms. It is encouraging that using the derived micromechanical model, we can explain volume change, transition from “brittle” to “ductile” and failure behavior of cohesive materials under multi-axial loading, even though we have utilized relatively simple descriptions of inter-granular behavior. How the different inter-granular mechanisms contribute to the overall deformation and failure response needs further exploration and is part of our on-going investigation with this model. In addition, our future work will comprise of model performance evaluation under loading paths that incorporate shear stresses and extending the model to include the effect of unloading as well as cyclic loading.

## Acknowledgements

Work reported in paper includes that done by former students Prapon Somboonyanon and Pavan Lakku. This work was also partially supported by a NASA EPSCOR Partnership DevelopmentGrant.

## References

Balmer, G.G., 1949. Shearing strength of concrete under high triaxial stress-computation of Mohr’s envelope as a curve. Structural Research Laboratory Report No. SP-23. Bureau of Reclamation, United States of the Interior.

Bažant, Z.P., Caner, F.C., 2005. Microplane model M5 with kinematic and static constraints for concrete fracture and anelasticity. I: theory. Journal of Engineering Mechanics 131 (1), 31–40.

Chang, C.S., Misra, A., 1990. Packing structure and mechanical properties of granulates. Journal of Engineering Mechanics 116 (5), 1077–1093.

Chang, C.S., Lun, M., 1992. Elastic material constants for isotropic granular solids with particle rotation. International Journal of Solids and Structures 29 (8), 1001–1018.

Chang, C.S., Liao, C.L., 1994. Estimates of elastic modulus for media of randomly packed granules. Applied Mechanics Review 47 (1), 197–206.

Chang, C.S., Gao, J., 1996. Kinematic and static hypotheses for constitutive modeling of granulates considering particle rotation. Acta Mechanica 115, 213–229.

Chang, C.S., Askes, H., Sluys, L.J., 2002. Higher-order strain/higher-order stress gradient models derived from a discrete microstructure, with application to fracture. Engineering Fracture Mechanics 69 (17), 1907–1924.

Chang, C.S., Hicher, P.Y., 2005. An elasto-plastic model for granular materials with microstructural consideration. International Journal of Solids and Structures 42 (14), 4258–4277.

Ferretti, E., 2004. Experimental procedure for verifying strain-softening in concrete. International Journal of Fracture 126, 27–34.

Gao, H., Klein, P., 1998. Numerical simulation of crack growth in an isotropic solid with randomized internal cohesive bonds. Journal of Mechanics and Physics of Solids 46 (2), 187–218.

Gopalaratnam, V.S., Shah, S.P., 1985. Softening response of plain concrete in direct tension. ACI Journal 82 (3), 310–323.

Hicher, P.Y., Chang, C.S., 2005. Evaluation of two homogenization techniques for modeling the elastic behavior of granular materials. Journal of Engineering Mechanics 131, 1184–1194.

Hicher, P.Y., Chang, C.S., Dano, C., 2008. Multi-scale modeling of grouted sand behavior. International Journal of Solids and Structures 45 (16), 4362–4374.

Jaeger, J.C., Cook, N.G.W., Zimmerman, R.W., 2007. Fundamentals of Rock Mechanics, forth ed. Blackwell Punlishing, Malden, MA.

Jefferson, G., Haritos, G.K., McMeeking, R.M., 2002. The elastic response of a cohesive aggregate – a discrete element model with coupled particle interaction. Journal of the Mechanics and Physics of Solids 50, 2539–2575.

Israelachvili, J.N., 1985. Intermolecular and Surface Forces. Academic Press, New York.

Kupfer, H., 1973. Das verhalten des betons unter mehrachsiger kurzzeitbelastung unter besonderer berücksichtigung des zweiachsiger beanspruchung (Behavior of concrete under multiaxial short term loading, with emphasis on biaxial loading). Deutscher Ausschuss für Stahlbeton, vol. 229, Berlin, German.

Lin, P., Shu, Chi-Wang, 2002. Numerical solution of a virtual internal bond model for material fracture. Physica 167, 101–121.

Misra, A., Chang, C.S., 1993. Effective elastic moduli of heterogeneous granular solids. International Journal of Solids and Structures 30 (18), 2547–2566.

Misra, A., 2002. Effect of asperity damage on friction behavior of single fracture. Engineering Fracture Mechanics 69 (17), 1997–2014.

Misra, A., Thiagarajan, G., Somboonyanon, P., 2003. Pseudo particle-potential model for granular materials. In: The Electronic Proceedings of the 16th ASCE Engineering Mechanics Conference, Seattle, WA, <http://www.ce.washington.edu/em03/proceedings/papers/406.pdf>, (July 2003).

Misra, A., Ouyang, L., Chen, J., Ching, W.Y., 2007. Ab Initio calculations of strain fields and failure patterns in silicon nitride intergranular glassy films. Philosophical Magazine 87 (25), 3839–3852.

Murrell, J.N., Carter, S., Farantos, S.C., Huxley, P., Varandas, A.J.C., 1984. Molecular Potential Energy Functions. John Wiley, New York.

Szlufarska, I., Nakano, A., Vashishta, P., 2005. A crossover in the mechanical response of nanocrystalline ceramics. Science 309, 911–914.

van Mier, J.G.M., 1984. Strain-softening of concrete under multiaxial loading conditions. Ph.D. Thesis, Eindhoven University of Technology, The Netherlands.

van Mier, J.G.M., 1986. Multiaxial strain-softening of concrete. Materials and Structures 19, 190–200.

van Mier, J.G.M., Shah, S.P., Arnaud, M., Balayssac, J.P., Bascoul, A., Choi, S., Dasenbrock, D., Ferrara, G., French, C., Gobbi, M.E., Karihaloo, B.L., Konig, G., Kotsovos, M.D., Labuz, J., Lange-Kornbak, D., Markeset, G., Pavlovic, M.N., Simsch, G., Thienel, K-C., Turatsinze, A., Ulmer, M., van Geel, H.J.G.M., van Vliet, M.R.A., Zissopoulos, D., 1997. Strain-softening of concrete in uniaxial compression. Materials and Structures 30, 195–209.

van Mier, J.G.M., 1997. Fracture Processes of Concrete. CRC Press, Boca Raton, FL.

van Mier, J.G.M., 2007. Multi-scale interaction potentials (*F*–*r*) for describing fracture of brittle disordered materials like cement and concrete. International Journal of Fracture 143, 41–78.

Volokh, K.Y., Gao, H., 2005. On the modified virtual internal bond method. Journal of Applied Mechanics 72, 969–971.

Xie, J., Elwi, A.E., MacGregor, J.G., 1995. Mechanical properties of three high-strength concretes containing silica fume. ACI Materials Journal 92 (2), 135–145.

Yin, W.S., Eric, C.M.S., Mansur, M.A., Hsu, T.C.T., 1989. Biaxial tests of plain and fiber concrete. ACI Materials Journal 86 (3), 236–243.

Zhang, Z.N., Ge, X.R., 2005. Micromechanical consideration of tensile crack behavior based on virtual internal bond in contrast to cohesive stress. Theoretical and Applied Fracture Mechanics 43, 342–359.

Zhang, Z.N., Ge, X.R., 2006. A multiscale mechanical model for materials based on virtual internal bond theory. Acta Mechanica Solida Sinica 19 (3), 197–202.

Zhang, Z.N., Ge, X.R., 2008. Numerical simulation of two-dimensional shear fracture based on virtual multi-dimensional internal bonds. International Journal of Rock Mechanics and Mining Sciences 45, 442–459.

Zhou, Y.X., Wang, Y., Mallick, P.K., Xia, Y.M., 2004. Strain softening constitutive equation for tungsten heavy alloy under tensile impact. Materials Letters 58 (22–23), 2725–2729.